

RESEARCH

Open Access



Novel plasmon-coupled Ag/Ag₂O nano-particles to downregulate β -catenin pathway in triple negative breast cancer

A. Kamal Mohamed¹, S. I. El-Dek^{1*}, Saad M. EL-Gendy² and Ahmed. A. G. El-Shahawy¹

*Correspondence:
samaa@psas.bsu.edu.eg

¹ Materials Science and Nano Technology Department, Faculty of Postgraduate Studies for Advanced Sciences, Beni-Suef University, Beni-Suef, Egypt

² Cancer Biology Department, National Cancer Institute, Cairo University, Cairo, Egypt

Abstract

We prepared novel plasmon-coupled silver (Ag) and silver oxide (Ag₂O) nanoparticles using green synthesis and a magnetic stirrer device from lemon juice. Firstly, we prepared six Ag samples from green tea and lemon juice, characterized by XRD, FTIR, UV, and HRTEM. We selected just two samples to apply to MDA-MB-231 cells. The samples entered the cell through endocytosis, showed moderate cytotoxicity and ROS levels, caused cell growth arrest at the G2M phase, exhibited higher inhibition of Cyclin D1, and induced early apoptosis. β -Catenin is an abundant protein in triple-negative breast cancer TNBC. Both samples showed inhibition of the β -catenin proteins pathway. Plasmon-coupled nanoparticles effectively inhibited β -catenin, physically capturing β -catenin and its pathway proteins, mimicking the action of a degradation protein complex due to their geometric properties. The prepared materials could be considered a promising treatment for TNBC that has not responded to chemotherapy and radiotherapy. As they have low toxicity to normal cells; this paves the way for new material designs without strict size limitations.

Keywords: Plasmon coupling, Green synthesis, Ag nanoparticles, Beta-catenin, TNB, Cancer

Introduction

Breast cancer has been a life-threatening disease among women over the decades. Scientists' efforts intensify daily to combat the cancer malignancy. The current treatments for breast cancer are chemotherapy, radiotherapy, and targeted therapies. Unquestionably, chemotherapeutic agents have several limitations due to their higher toxicity to normal cells. Recently, scientists discovered that only a small proportion of cancer cells control the entire population. These master cells are called cancer stem cells, tumor-initiating cells, or "CSCs" and are responsible for tumor initiation, propagation, and metastasis (Xu et al. 2015).

TNBCs like MDA-MB-231 are more resistant to chemotherapy and radiotherapy than other breast cancer types. Due to the high expression of certain biological pathways, such as the canonical β -catenin pathway, notch, and hedgehog pathways, those pathways



© The Author(s) 2024. **Open Access** This article is licensed under a Creative Commons Attribution 4.0 International License, which permits use, sharing, adaptation, distribution and reproduction in any medium or format, as long as you give appropriate credit to the original author(s) and the source, provide a link to the Creative Commons licence, and indicate if changes were made. The images or other third party material in this article are included in the article's Creative Commons licence, unless indicated otherwise in a credit line to the material. If material is not included in the article's Creative Commons licence and your intended use is not permitted by statutory regulation or exceeds the permitted use, you will need to obtain permission directly from the copyright holder. To view a copy of this licence, visit <http://creativecommons.org/licenses/by/4.0/>.

express many proteins responsible for cancer progression (Dittmer 2018). β -Catenin is a protein encoded in human cells by the CTNNB1 gene, and it is a member of the cadherin protein complex, a transmembrane protein divided into two parts: extracellular and intracellular. The role of the extracellular part in cell–cell adhesion; it binds calcium ions and forms dimers with others to create extracellular junctions. The second part is to function as an intracellular signal transducer for the transcription of certain genes crucial for cancer propagation (Cheng et al. 2019). β -Catenin has an important role in the tumorigenicity of TNBC and is involved in stem cells, proliferation, metastasis, and sensitivity to chemotherapy.

The Wnt β -catenin signaling pathway, also known as the canonical Wnt pathway, operates in two states: on and off. In the off state, the Wnt ligand does not bind to the frizzled receptor (Wong et al. 2018; Rana et al. 2019; Wahab et al. 2019). This triggers the assembly of the degradation protein complex, which includes four proteins: APC (adenomatous polyposis coli), GSK3 β (glycogen synthase kinase 3 beta), CK1 (casein kinase 1 alpha), and Axin. β -Catenin, when surrounded by this complex, undergoes phosphorylation. It then interacts with the B-TRCP enzyme, which adds ubiquitin groups to β -catenin. Ubiquitination marks β -catenin for degradation by proteasomal enzymes, leading to a decrease in its cytoplasmic levels. In the "on stage" of the Wnt β -catenin signaling pathway, the Wnt ligand binds to the frizzled receptor, a G-protein coupled receptor with seven transmembrane helices. This binding leads to the recruitment of Dishevelled (DVL or DSH) protein to the intracellular side of the frizzled receptor. In addition, the LRP5 and LRP6 co-receptors become phosphorylated. Part of the degradation protein complex, including GSK3 and axin, translocates to the receptor complex, preventing the phosphorylation of β -catenin. As a result, β -catenin accumulates freely in the cytoplasm without being targeted for degradation by proteasomes, leading to an increase in its cytoplasmic levels. A larger portion of β -catenin then translocates into the nucleus (Yu et al. 2020).

Green synthesis is eco-friendly and generates materials with low toxicity (Huang et al. 2019). Due to their unique chemical, physical, and optical properties, silver nanoparticles AgNPs have a wide range of applications, including antimicrobial activity (Haq et al. 2018), enhanced conductivity, and optical properties, so they are used in "plasmonics." Further AgNPs exhibit a unique phenomenon called surface plasmon resonance, which enables them to be multifunctional materials as an optical biosensing probe in breast cancer (Salahandish et al. 2018; Hassanpour et al. 2019; Han et al. 2021; Yoo et al. 2021). Silver oxide nanoparticles, Ag₂ONPs, attract significant attention for their applications in photocatalysis and semiconducting materials. They are noted for their higher chemical stability compared to AgNPs. Medical applications of metallic silver (Ag) are currently limited due to concerns about its toxicity. Capping and designing silver nanoparticles (AgNPs) can help mitigate these toxicity concerns, making them potentially safer for medical use (Juganson et al. 2015).

In our current research, we synthesized AgNPs using two methods green tea and lemon extract. The plasmon coupling was observed in most of our preparations. As plasmon–plasmon, plasmon–phonon, plasmon photon, plasmon–magnon couplings and polaritons are the coming era; we selected two types for our biological applications: individual particles approximately 19 nm in size and plasmon-coupled Ag/Ag₂ONPs around

50 nm in size. The selection criteria include distinguishing between well-dispersed AgNPs and plasmon-coupled ones when applied to MDA-MB-231 cells, particularly focusing on the β -catenin protein. Our objective was to evaluate the effectiveness of two preparations—AgNPs synthesized using green tea or lemon extract—on MDA-MB-231 cells. We aimed to demonstrate that the design and composition of the material play a crucial role in its effectiveness, potentially overshadowing the importance of nanoparticle size alone. Our results showed that plasmon-coupled nanoparticles (50 nm) were more effective for treating TNBC than smaller particles.

Materials and methods

Materials

The materials used in our experiments included silver nitrate (AgNO_3) from ALAMIA COMPANY FOR CHEMICALS, Pluronic[®] F-68 (plant cell culture tested), and BioReagent polyoxyethylene–polyoxypropylene block copolymer from SIGMA, all used without further purification. In a typical experiment, silver nanoparticles were prepared via green synthesis using green tea extract and lemon juice in six different environments: three from green tea (T1, T2, and T3) and three from lemon juice (L1, L2, and L3) using a magnetic stirrer. The details for the green tea experiments:

Green Tea Experiment [T1]: Green tea extract was prepared by adding 5.985 g of green tea to 50 ml of distilled water at 80 °C for 15 min. 0.5 g of AgNO_3 was dissolved in 250 ml of distilled water using a magnetic stirrer. 10 ml of the green tea extract was added dropwise to the AgNO_3 solution and stirred for 24 h at 160 rpm. **Green Tea Experiment [T2]:** Green tea extract was prepared by adding 1.8 g of green tea to 50 ml of distilled water at 80 °C for 15 min. Afterward, 1.02 g of AgNO_3 was combined with 1.02 g of Pluronic F68 in 500 ml of distilled water using a magnetic stirrer. Subsequently, 25 ml of green tea extract was added dropwise to the solution and stirred for 24 h at 100 rpm. **Green Tea Experiment [T3]:** Green tea extract was prepared with 5.9 g of green tea added to 50 ml of distilled water at 80 °C for 15 min. 1.66 g AgNO_3 was added to 1.66 g Pluronic F68 in 110 ml of dissolved water by a magnetic stirrer, and then 30 ml of green tea extract was added dropwise and stirred for 24 h at 160 rpm.

The details for the lemon juice experiments are:

Lemon Juice Experiment [L1]: Fresh citrus fruits from Egypt were washed with distilled water, cut into small pieces, squeezed, and filtered through normal filter paper to obtain concentrated lemon juice. 0.176 g of AgNO_3 was added to 100 ml of distilled water. 10 ml of lemon juice was added dropwise to the AgNO_3 solution and stirred for 24 h at 800 rpm. **Lemon Juice Experiment [L2]:** 1.69 g of AgNO_3 was added to 1000 ml of distilled water. 100 ml of lemon juice was added dropwise to the AgNO_3 solution and stirred for 24 h at 800 rpm. **Lemon Juice Experiment [L3]:** 1.70 g of AgNO_3 was added to 110 ml of distilled water. 1.72 g of Pluronic F68 was also added to the solution. 80 ml of lemon juice was added dropwise to the mixture and stirred for 24 h at 160 rpm (Table 1). It is worth hinting that in the seventh preparation (L3 repeated with aged polymer), the conditions were identical to L3, except that the Pluronic polymer used in this preparation had been physically aged. This aging process involved storing the polymer in a

Table 1 Flow cytometric data of (A) apoptosis, (B) cell cycle and (C) ROS of T2, L3 treated cells and control MDA-MB-231 cells

A	Sample	Tested conc. ($\mu\text{g}/\text{ml}$)	Early apoptosis	Last apoptosis	Necrosis	
	T2 (Treated cells)	0.93	1.94	27	15.32	
	L3 (Treated cells)	17.2	3.06	8.78	7.21	
	MDA-MB-231 cells (control)	0	0.49	0.15	1.2	
B	Sample	Tested conc. ($\mu\text{g}/\text{ml}$)	% G0–G1	% S	% G2–M	% Pre G1
	T2 (Treated cells)	0.93	55.03	41.92	3.05	44.26
	L3 (Treated cells)	17.2	41.36	37.26	21.38	19.05
	MDA-MB-231 cells (control)	0	46.04	41.26	12.7	1.84
C	Sample	Tested conc. ($\mu\text{g}/\text{ml}$)	ΔRFU	% of control		
	T2 (Treated cells)	0.93	176,762.407	138.44		
	L3 (Treated cells)	17.2	164,754	129.02		
	MDA-MB-231 cells (control)	0	127,691.958	100		

falcon tube for approximately 2 years, during which its color changed from snow white to pale yellow. The synthesized AgNPs in this experiment were not preserved in liquids or buffers; they were completely separated from the media and then dried, primarily by freezing (Table S1).

Characterizations

The characterizations of the nanoparticles were conducted as follows:

Morphological studies using the High-Resolution Transmission Electron Microscope (Jeol.jem.2100, Japan) and Carl Zeiss (Germany), model: Zeiss Sigma 500 VP Analytical FE-SEM. Fourier transformation infrared spectroscopy (FTIR) by A. Bruker (Vertex 70 FTIR–FT Raman). UV–Vis spectroscopy (Shimadzu UV–visible spectrophotometer). Magnetic measurements (VSM LakeShore 7410, USA) with a maximum applied field of 20 kOe at room temperature. X-ray diffraction, the XRD technique, was used to characterize the crystallinity of the materials using Cu K α radiation ($\lambda = 1.54 \text{ \AA}$). The instrument was operated with a current of 35 mA, an operating voltage of 40 kV (power 1200 W), and a scanning speed of 2/min (step size = 0.05° and step time = 1.5 s) in the 10–70 scanning range (2 θ scale).

Biochemical assays

The MTT viability assay was conducted to evaluate the cytotoxicity of T2 and L3. MDA-MB-231 cells, a human breast cancer cell line from the American Type Culture Collection (ATCC, Rockville, MD), were incubated with these nanoparticles for 24 and 48 h. Optical density was measured at 590 nm using a microplate reader (SunRise, TECAN, Inc., USA). In addition, MDA cells treated with T2, L3, and control cells were examined under a JEOL 1010 Transmission Electron Microscope (JEOL Ltd., Tokyo, Japan) at

80 kV. Digital photographs were captured using a Hamamatsu digital camera C4742-57-12NR (Hamamatsu, Japan).

Flow Cytometry Assays: (i) Apoptosis analysis (Annexin V-FITC assay) was analyzed using the flow cytometer BD FACS Calibur (BD Biosciences, San Jose, CA). (ii) Cell cycle analysis was done using the CycleTEST™ PLUS DNA Reagent Kit (Becton Dickinson Immunocytometry Systems, San Jose, CA). The cell cycle analysis was performed using Cell Quest software (Becton Dickinson Immunocytometry Systems, San Jose, CA). (iii) ROS determination The ROS was measured at 520 nm using the Invitrogen Total Reactive Oxygen Species (ROS) Assay Kit (88–5930, Thermo Fisher Scientific Inc.).

Western blot assay: The primary antibodies against BAX (1:1000, Cell Signaling Technology), Bcl-2 (1:1500, Cell Signaling Technology), and Cytochrome c (1:500, Santa Cruz Biotechnology) cleaved caspase-3 (1:750, Cell Signaling Technology), caspase-9 (1:1500, Cell Signaling Technology), p53 (1:1000, Abcam), and β -actin (1:5000, Sigma) The primary antibodies against β -Catenin (1:1500, Cell Signaling Technology), c-Myc (1:1000, Cell Signaling Technology), Cyclin D1 (1:5000, Abcam), and β -actin (1:5000, Sigma) were used. The total proteins were determined by colorimetric methods using the Bradford method. DNA fragmentation data by gel electrophoresis: band observations under the UV transilluminator were done according to the gel documentation system (BIO-RAD, Gel Doc 2000). The VEGF assay (Vascular endothelial growth factor receptor 2, “VEGFR2”) is assayed by ELIZA technology using the VEGFR2 (KDR) Kinase Assay Kit (Catalogue # 4032), text S2.

Results and discussion

XRD diffraction patterns

Figure 1a illustrates the XRD patterns of the prepared samples using green tea extract. The data were compared with JCPDS file no. (1100136 QM: C) of cubic Ag. The patterns were composed of four main reflections. The located peaks at 2 theta values (38.14, 44.31, 64.52, and 77.45) were indexed as (111, 200, 220, and 311), respectively. This analysis agreed with that reported for the synthesized AgNPs (Lotfy et al. 2021; Xu et al. 2017). The peak width and intensity were found to depend on the preparation conditions. The samples exhibited excellent crystallinity despite their small size.

The value of the crystallite size was calculated from the well-known Debye–Scherrer equation, $L = \frac{K\lambda}{\beta \cos\theta}$ where K is the shape factor = 0.9, λ is the X-ray Cu target wavelength = 1.5406 Å, and β is the corrected full width at half maximum of the most intense peak located at θ . The results revealed that the crystallite sizes for the samples were as follows: Sample T1: 30 nm, Sample T2: 50 nm, Sample T3: 30 nm.

Figure 1b shows the XRD patterns of the prepared samples using lemon juice extract exhibited crystallization into two phases. The first phase is cubic silver (Ag) with mean 2 θ values at 38.10°, 44.24°, 64.44°, and 77.4°, indexed as (111), (200), (220), and (311) respectively for L1, L2, and L3. The second phase is hexagonal silver oxide (Ag₂O) with mean 2 θ values at 17.86°, 33.67°, 36.31°, 38.40°, 50.38°, 60.20°, 66.71°, 72.32°, and 73.72°, indexed as (001), (100), (002), (011), (102), (110), (103), (112), and (201) respectively for L1, L2, and L3 (Tseng et al. 2010; Raju et al. 2009). The presence of both phases is confirmed by the splitting and broadening of the XRD reflections, as shown in the inset of Fig. 1b.

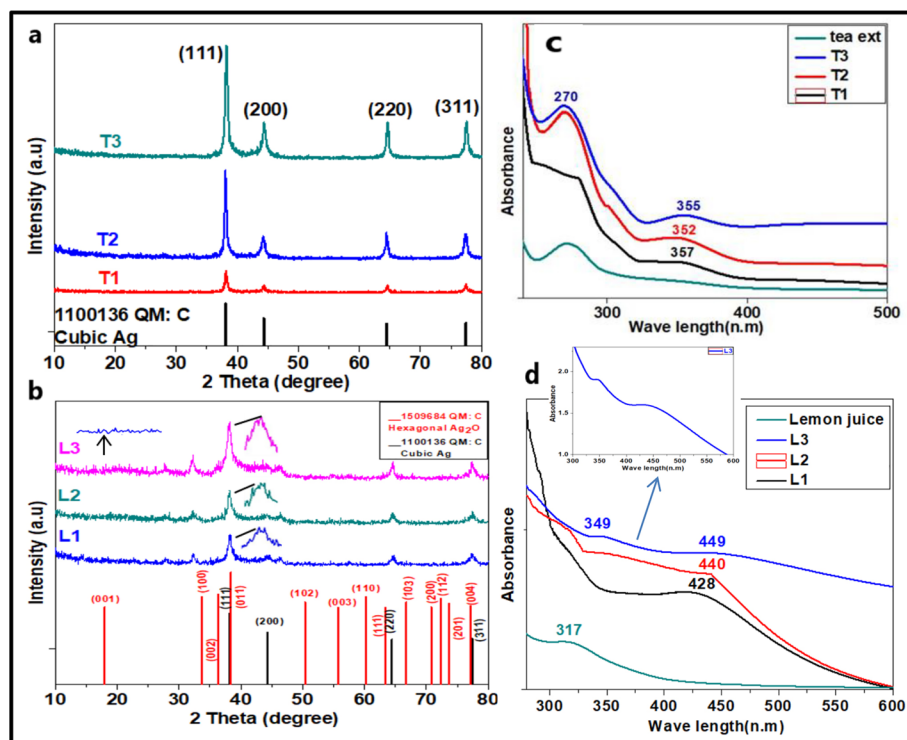


Fig. 1 a, b XRD patterns of the prepared samples and c, d UV spectroscopic data of the prepared silver samples T1, T2, T3, tea extract, L1, L2, L3, and lemon juice

As expected, the AgNPs transformed oxidation into Ag₂O due to their large surface area. The observed broad and low-intensity XRD peaks reflect the characteristics of tiny-sized nanoparticles, resembling an erratic electrocardiogram. The XRD data were indexed using JCPDS card no. 1100136 QM: C for the cubic phase (Ag) and 1509684 QM: C for the hexagonal phase (Ag₂O), consistent with previous studies (Tseng et al. 2010; Abdullah et al. 2015). Peaks observed at 32.26°, 32.36°, and 32.27° for L1, L2, and L3, respectively, suggest the presence of cubic Ag₂O polymorphs (Algahtani et al. 2022). Therefore, samples L1, L2, and L3 can be considered nanocomposite Ag/Ag₂O, where polymorphism indicates the presence of the same compound in different crystal structures within the same preparation (Sophia et al. 2020).

Ultraviolet spectroscopic data

The absorbance peak of AgNPs is reported to be within the range of 420–450 nm (Kaplan et al. 2022), while Ag₂ONPs have an absorbance peak in the range of 400–500 nm (Geng et al. 2017; Korkmaz and Karadağ 2021). Plasmon coupling occurs when two plasmonic metal particles, such as silver or gold, approach each other at a distance smaller than the diameter of either particle. This proximity leads to hybridization of the surface plasmon resonance (SPR), resulting in a shift in the UV absorbance spectrum, which can manifest as either a blue or red shift.

A red shift occurs when the coupling is longitudinal and the distance between the particles is greater than 1 nm, following classical electromagnetic theories. Conversely, a blue shift occurs with transverse coupling when the distance between particles is less

than 1 nm, introducing quantum effects that cause the particles to deviate from classical rules (Cha et al. 2016). Figure 1c, d illustrates the SPR λ_{\max} for the samples prepared with green tea: T1: 357 nm, T2: 352 nm, T3: 355 nm, and Tea extract: 270 nm. Based on XRD and HRTEM data, T1 and T3 exhibit transverse plasmon coupling between cubic–cubic Ag nanoparticles. T2, however, does not show evidence of plasmon coupling.

The blue shift of the peak below 400 nm can be attributed to two main factors:

The 1st Particle Size: The smaller size of T2 (19.0 nm) compared to T1 and T3 (83.7 nm and 99.4 nm, respectively) contributes to the blue shift. Smaller nanoparticles tend to exhibit blue shifts in their SPR peaks. **The 2nd Residual Energies:** all samples were measured immediately after being removed from the magnetic stirrer device and before separation by centrifugation. This timing means they may still retain some electromagnetic and kinetic energies transferred by the magnetic stirrer device, influencing the observed shift. These factors together explain the observed blue shift in the SPR peaks of the samples.

Considering the lemon juice experiments, the SPR λ_{\max} values are: L1: 428 nm, L2: 440, L3: 349 and 449 nm, Lemon juice: 317 nm. For L1: contains cubic Ag as the first crystal phase and hexagonal Ag₂O NPs as the second crystal phase. The absorbance λ_{\max} at 428 nm refers to cubic AgNPs, potentially indicating longitudinally disorganized coupling. For L2: exhibits a λ_{\max} at 440 nm and contains cubic Ag crystals, appearing in HRTEM micrographs as a core–shell structure with a rounded core and a thick shell, as shown in Fig. 3.

The localized SPR of a shell is primarily influenced by the diameter of the shell and the dielectric properties of the core. As the shell thickness increases, the localized SPR shifts to higher wavelengths (a "red shift") (Jain and El-Sayed 2010). This explains the λ_{\max} at 440 nm for sample L2, as the increased shell thickness causes this redshift. For sample L3: it has two peaks: one at 349 nm, corresponding to the transverse plasmon coupling of the particles, and another at 449 nm, which is the original absorbance peak of AgNPs. The coupling at 349 nm is likely between cubic–cubic particles or hexagonal–cubic particles. There is greater enhancement of the electromagnetic field at the corners and edges of polygon shapes compared to spherical shapes due to the excitation of localized SPR (Tanimoto et al. 2015), which facilitates the formation of hexagonal–cubic coupling.

FTIR spectra interpretation

Figure 2a–d displays the FTIR spectra of the prepared materials. In the AgNPs prepared from tea extract, a comparison between T1 and the tea extract, both measured as aqueous samples, revealed differences in certain wavenumber bands, either through the presence of new bands or threshold differences. Figure 2a shows the IR transmission bands for T1 at 3820.1, 3275.0, 2998.0, 1637.0, 1396.3, 1205.0, 1062.8, and 619.0 cm⁻¹ (Table S3). The bands at 3820.1 cm⁻¹ and 2998.0 cm⁻¹ were present in T1 but absent in the tea extract. In addition, there was a threshold difference in wavenumbers; bands at 1396.3 cm⁻¹ and 1062.8 cm⁻¹ in T1 were higher than those in the tea extract. For T2 and T3, both prepared with PLF68: Fig. 2b shows T2 with four intensive IR bands at 3410.3, 1600.8, 1358.7, and 1070.3 cm⁻¹. T3 has two intensive bands at 1601.3 and 1076.0 cm⁻¹.

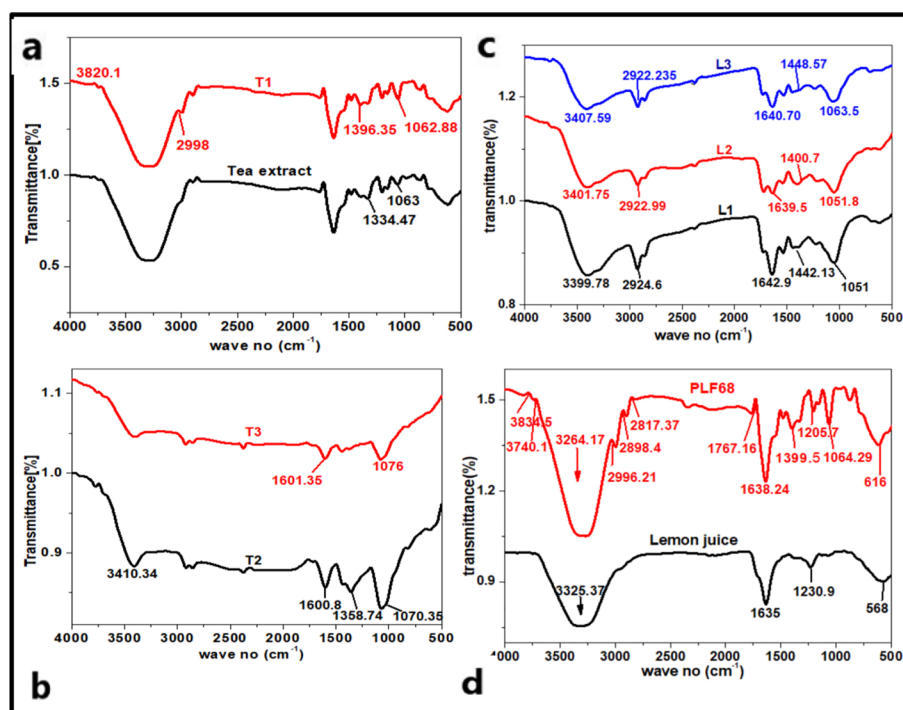


Fig. 2 FTIR spectrum data of the prepared samples. **a, d** Measured as aqueous samples. **c, b** Measured as solid samples

The peaks at 1070.3 cm^{-1} and 1076.0 cm^{-1} for T2 and T3, respectively, correspond to C–C vibrations due to the presence of PLF68, and they shift slightly from the original band of the polymer (1064 cm^{-1}), likely due to the capping of the silver NPs. All three preparations indicate the formation of cubic silver NPs (Jinu et al. 2017; Syed et al. 2019).

Figure 2c displays the FTIR data of the prepared Ag NPs from lemon juice. The following observations were peaks at 1442.0 cm^{-1} (L1), 1400.7 cm^{-1} (L2), and 1448.5 cm^{-1} (L3) were assigned to the prepared Ag_2ONPs (Algahtani et al. 2022). According to Mostafa et al. (Hosseinpour-Mashkani and Ramezani 2014), cubic Ag was observed at 3431 and 1647 cm^{-1} , while hexagonal Ag_2ONPs were observed at 3432 and 1638 cm^{-1} . Bands at 3399.7 cm^{-1} , 3401.7 cm^{-1} , 3407.5 cm^{-1} , 1642.9 cm^{-1} , 1639.5 cm^{-1} , and 1640.7 cm^{-1} were assigned to the (OH) stretching and bending vibrations of hexagonal Ag_2O NPs for L1, L2, and L3, respectively. Bands at 2924.6 cm^{-1} (L1), 2922.9 cm^{-1} (L2), and 2922.2 cm^{-1} (L3) referred to the CH_2 antisymmetric stretching of the prepared cubic Ag NPs (Jinu et al. 2017; Syed et al. 2019). Bands at 1051.0 cm^{-1} (L1), 1051.8 cm^{-1} (L2), and 1063.0 cm^{-1} (L3) were assigned to the C–C vibrations, with shifts in L3 likely due to the presence of the PLF68 polymer, indicating possible capping of the particles. The FTIR data supports the XRD data, showing that T1–T3 has one crystal family phase, while L1–L3 has at least two crystal family phases.

We measured the zeta potential of the samples T2 and L3. The T2 sample showed a zeta potential of approximately -12.0 mV , based on triplicate measurements of -12.5 , -12.1 , and -11.5 mV . For the L3 sample, the zeta potential was around -13.0 mV , with triplicate measurements of -12.9 , -13.5 , and -12.7 mV (Figure S4).

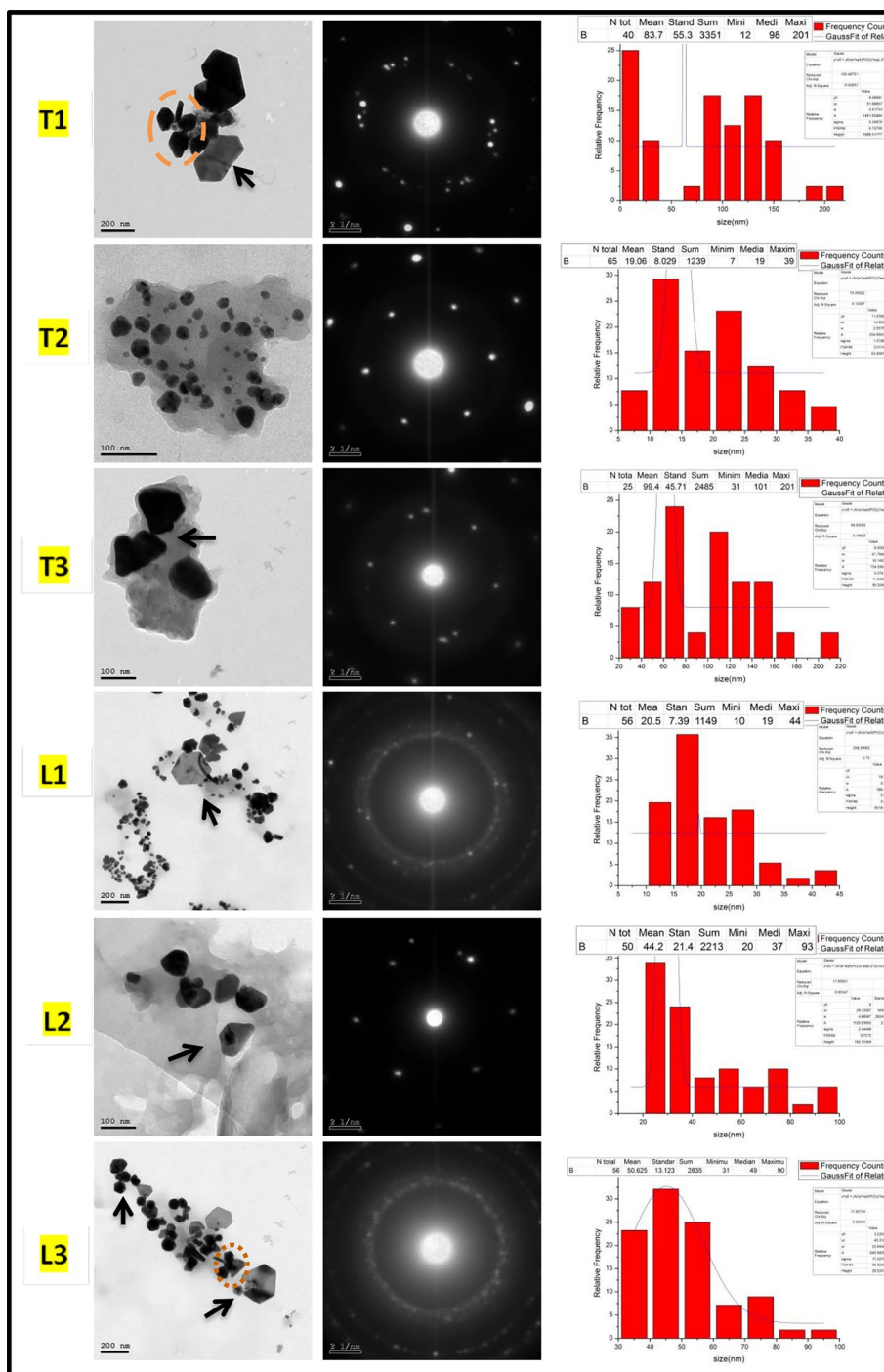


Fig. 3 HRTEM of the prepared six silver samples T1, T2, T3, L1, L2, and L3 followed by SAED patterns and size distribution graphs for each sample

High-resolution transmission *electron* microscopy

Figure 3 shows HRTEM images, selected area electron diffraction patterns, and size distribution histograms of the prepared samples. The micrographs confirmed the formation of AgNPs in various geometric shapes depending on the reducing agent type and its concentration. This indicates that preparation conditions are crucial in

controlling the final product of AgNPs. For the samples prepared with tea extract, T1 and T3 are similar as they both display crystal-twinned particles. In sample T1, there are two pentahedral shapes of Ag nanoparticles tightly bound through a twin plane (mirror plane), a phenomenon known as "crystal twinning."

This phenomenon occurs when the material is subjected to temperature and/or pressure, as in our samples prepared under magnetic stirring. In sample T3, there are crystal twins: one heart-shaped and the other inverted heart-shaped AgNPs, but they are not fully tightly bound to each other, and the twin plane does not appear perfectly. These multiple twinned particles indicate that the preparation method with a magnetic stirrer provides a suitable environment for the particles to be close to each other, favoring twin formation. Sample T2 shows separated particles, mostly rounded and well dispersed due to the Pluronic F68 copolymer and the large preparation volume (500 ml). HRTEM findings confirm that the particle shape and geometry of AgNPs synthesized using green tea extract are the main factors behind the plasmon coupling formation observed in T1 and T3.

For the samples prepared using lemon juice, L1 and L3 exhibit a hexagonal shape, while L2 predominantly features a triangular shape. Sample L1 likely contains longitudinally coupled particles ($\lambda = 428$ nm) (Arve et al. 2006). Sample L2 displays a core-shell-like morphology, with a silver core encased in a thick Ag₂O shell, which forms favorably in the highly acidic lemon juice medium. Sample L3 demonstrates plasmon coupling between Ag/Ag₂O nanoparticles (Cha et al. 2016; Huang et al. 2009) arranged in a preferred orientation. As a result, this creates a hot spot highly rich in electrical and magnetic fields. The core-shell structure of a triangular Ag nucleus and a primarily silver oxide shell is indicated by the arrow. The triangular shape represents the initial stage of nucleation. In sample L3, there are repeated shapes similar to those in T1, featuring three rounded particles and a rod between them, as observed before crystal growth (Suber 2018). In addition, sample L3 contains various polygons, including triangles, pentagons, hexagons, heptagons, and octagons (Ramesh et al. 2007).

The SAED of the samples prepared from green tea showed excellent crystallinity, indicated by the appearance of concentric rings, while the samples prepared from lemon juice exhibited lower crystallinity. The samples synthesized with green tea were generally larger, measuring 83.7 nm for T1 and 99.4 nm for T3, with T2 having a mean size of 19.0 nm. In contrast, the samples synthesized using lemon juice as a reducing agent revealed smaller sizes with better distribution and less coalescence, with mean sizes of 20.5 nm for L1, 44.2 nm for L2, and 50.6 nm for L3.

Scanning electron microscopy

SEM images are presented for samples T2 and L3 only. Sample T2 displays spherical-shaped particles due to the formation of cubic crystals of AgNPs. In contrast, sample L3 predominantly shows hexagonal Ag₂O structures stacked upon each other, resembling "a dumped rag structure." In addition, L3 features various distinct mat shapes of Ag₂O nanoparticles and spherical particles (mainly cubic silver) on its surface, arranged in circular and semicircular rings and connected by plasmon coupling phenomena (Fig. 4A). The ascorbic acid content in lemon juice might play a crucial role in the formation of

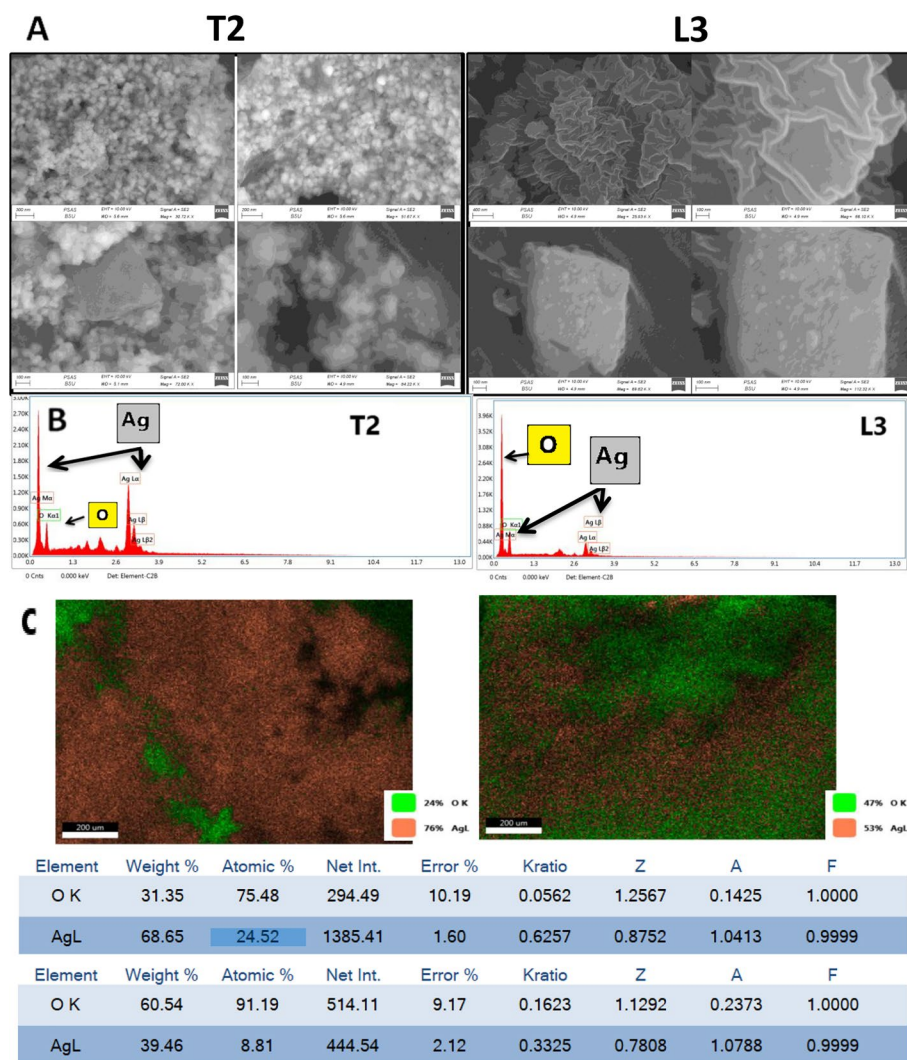
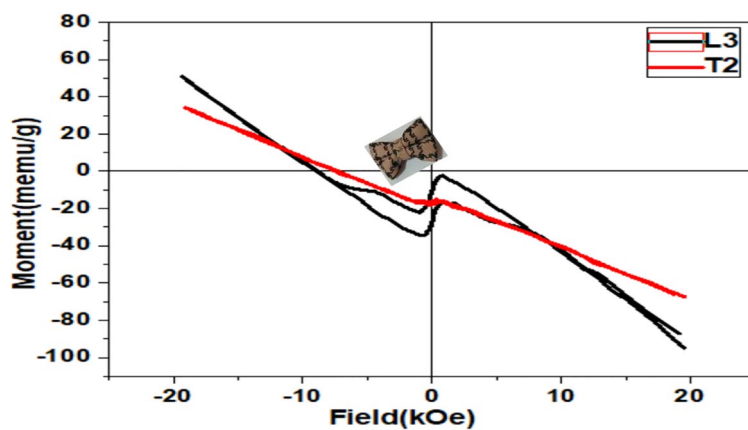


Fig. 4 SEM images of the chosen 2 samples T2 and L3 **A** for SEM images followed by **B** EDEX data and **C** mapping data of those two samples

the hexagonal shape resembling a "dumped rag" (Suber 2018). EDAX and mapping also confirm the phase purity and homogeneous distribution of elements in the investigated samples. EDAX and mapping clearly show that the oxygen content in L3 is higher than in T2, which aligns with the HRTEM micrographs and XRD findings (Fig. 4B, C).

Vibrating sample magnetometer

The magnetic properties of T2 and L3 were measured using a vibrating sample magnetometer (VSM). It is well known that silver is a diamagnetic material, with a susceptibility of 2.38×10^{-5} . According to Hoa Le Trong et al., silver can exhibit paramagnetic behavior upon the decomposition of silver oxalate (Le Trong et al. 2017). The data in Fig. 5 show that both samples are diamagnetic. However, the L3 sample displays some residual magnetization due to plasmon coupling between Ag and Ag₂O nanoparticles. The electron configuration of Ag⁴⁷ is [Kr]³⁶, 4d¹⁰, 5s¹, indicating



	T2	L3
Coercivity(Hci ,G)	116.88	3215.1
Maximum magnetization(Ms ,E-3emu)	50.777	72.933
Total area of hysteresis	2.4946 erg/g	107.92 erg/g

Fig. 5 VSM "Vibrating Sample Magnetometer" of T2 and L3

that the "d" orbital is filled with electrons. For pure silver, the Bohr magneton is zero, making it diamagnetic. When silver is oxidized, the Bohr magneton increases, slightly enhancing the diamagnetic properties. In the L3 sample, it is hypothesized that hexagonal Ag₂O nanoparticles are arranged with plasmon-coupled spherical cubic Ag, further influenced by the plasmon coupling effect.

The use of PLF68 polymer plays a significant role in the formation of couples and/or in the ordering of these couples in the preferred orientation of magnetization. The unpaired electrons in silver oxide form weak ferromagnetic clusters. Thus, the weak magnetization (ferromagnetic component) arises mainly from the collective behavior of three factors: (i) some induced oxygen vacancies at the interface between the coupled Ag/Ag₂O nanoparticles, creating a "frustrated spin glass" effect; (ii) the presence of a hot spot, which is the narrow space between two closely positioned particles causing surface plasmon resonance overlap, distinguished by magnetic flux lines (Tu and Wu 2021). (iii) The hexagonal crystalline structure of the Ag₂O nanoparticles enhances the preferred unique axis of magnetization (Tanimoto et al. 2015). These factors collectively result in a papillon-like or butterfly-shaped hysteresis loop (Tawfik et al. 2018). Upon using physically aged polymer, the EDAX data shows the sample composition includes 21% carbon, 11% oxygen, and 68% silver. The absorption λ_{max} is 340 nm, attributed to the plasmon coupling effect. The VSM does not show remaining magnetization in the hysteresis loop due to the lower content of oxide, resulting in fewer oxygen vacancies.

The couples formed, but the aged polymer could not order the particles in the preferred orientation, causing the electron magnetization to cancel each other out (Fig. 6). Although sample T2 has better crystallinity than sample L3, L3 shows remnant

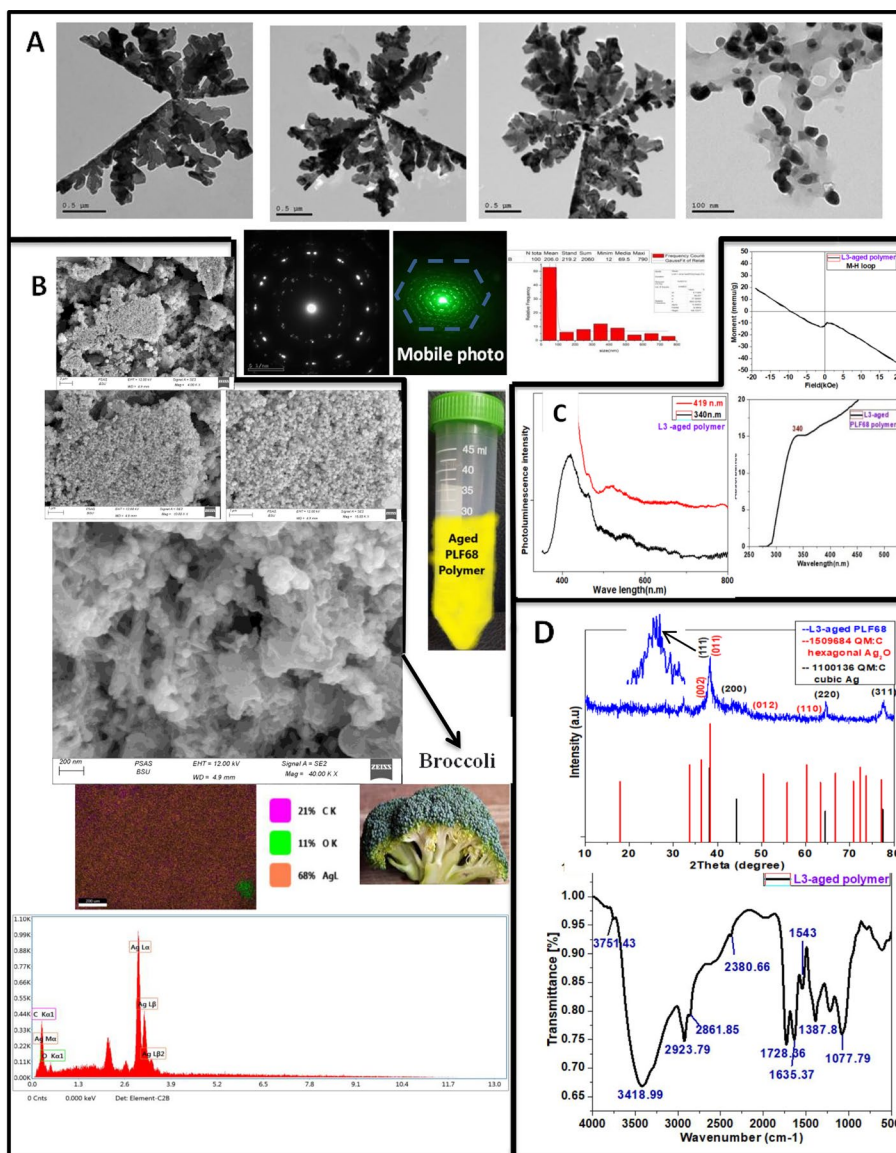


Fig. 6 L3 prepared by physically aged PLF68 polymer. **A** HRTEM images followed by SAED and size distribution graph. **B** SEM images followed by mapping and EDEX data. **C** photoluminescence, UV, and VSM curves. **D** XRD and FTIR data

magnetization. N. A. Toropov et al. reported that improving crystallinity doubles the dephasing time, an important parameter in the localized SPR (Toropov et al. 2018). The L3 sample is a promising material for the treatment of TNB cancer and other cancers in further studies (Ito et al. 2006; Vittorio et al. 2011).

Based on the above results and our preparation methods, three major factors contribute to the formation of plasmon coupling in our samples:

First, electromagnetic induction by magnetic stirrer: the magnetic stirrer operates on the principle of electromagnetic induction, a significant advancement in modern physics. It generates a magnetic field that causes a small rod magnet to rotate within the sample. This action promotes the alignment and coupling of particles in the sample.

Second, effect of ambient medium volume: the critical volume of the ambient medium plays a role in plasmon coupling formation. In general, as the volume of the ambient medium increases, the formation of plasmon coupling decreases. For example, samples T2 and L2, prepared in 500 ml and 1000 ml of distilled water respectively, show reduced plasmon coupling compared to T1, T3, L1, and L3, which were prepared in smaller volumes (250 ml, 110 ml, 100 ml, and 110 ml of distilled water respectively). Plasmon coupling arises from the presence of silver oxide alongside Ag nanoparticles. According to G. Cynthia Jemima Swarnavalli et al. (Joseph et al. 2011; Ahmed Al-Thabaiti et al. 2013), several factors influence the formation of hexagonal Ag nanoplates. These factors include reducing the reduction rate, using larger growth media, employing weak reducing agents like citric acid and ascorbic acid that encourage the formation of twinned seeds, and using capping agents that promote the development of a 2D plate-like structure. Silver oxide exhibits higher magnetic properties compared to elemental Ag. Polyhedral Ag₂O structures also exhibit higher localized SPR compared to spherical particles, making them more conducive to plasmon coupling formation.

Third, the use of polymers at specific concentrations plays a crucial role. The solution initially needs to be prepared as a supersaturated solution, which is energetically unstable. This instability leads to the formation of nuclei, which can be either homogeneous or heterogeneous (Burda et al. 2005). Subsequently, crystal growth occurs through the molecular addition of other molecules or aggregation with other particles. In sample L3, we observe two types of particles: hexagonal-shaped Ag₂O nanoparticles and cubic Ag nanoparticles, as mentioned earlier. The addition of a capping agent helps reduce Van der Waals forces between particles and mitigates their tendency to aggregate. The use of aged polymers facilitates continued crystal growth accompanied by flocculation (Tang et al. 2009).

Physically aged polymer refers to a polymer that has undergone an aging process due to exposure to environmental factors such as air or light over time. This aging process can lead to changes in the structure, composition, and properties of the polymer. In the context provided, the physically aged polymer used in the preparation of sample L3 had been aged for approximately 2 years in a falcon tube. As a result of this aging, the polymer's color changed from bright white to pale yellow. This aging process, whether chemical or physical, can significantly influence how the polymer interacts with other components in the preparation process, potentially affecting the characteristics and behavior of the final sample.

The oxidation of silver prepared using lemon juice can be attributed to its high acid content, specifically citric and ascorbic acids present in the preparation medium. When silver nitrate solution is added to the flask, silver nuclei precipitate out. These nuclei can subsequently oxidize, as seen in sample L2, due to the acidic nature of the lemon juice. According to Xiong and Xia (2007), mild reducing agents like citric acid or ascorbic acid can promote the formation of twinned seeds. When lemon juice, containing these weakly reducing agents, is introduced into the silver nitrate solution, silver seeds form. Some of these silver seeds undergo oxidation to silver oxide because of the acidity of the medium. Then the reaction medium triggers the formation of polyhedral Ag₂ONPs. The magnetic field generated by the magnetic stirrer facilitates the alignment of particles in a plasmon-coupled manner. Polyhedral Ag₂O nanoparticles (Ag₂ONPs) exhibit a higher

localized surface plasmon resonance (LSPR) compared to spherical nanoparticles. This enhanced LSPR in polyhedral Ag₂ONPs contributes to the efficient plasmon coupling observed in the nanocomposite structure. Based on our XRD, FTIR, UV, HR-TEM, and FE-SEM analyses of the Ag/Ag₂O nanocomposite in sample L3, we propose the following structure: a mat-like base of hexagonal Ag₂O nanoparticles coupled with smaller ring-shaped Ag nanoparticles (AgNPs) arranged in circular or hemi-circular rings. This configuration exhibits a novel plasmon coupling between the hexagonal-shaped Ag₂O nanoparticles and spherical cubic Ag ones.

Biology assays

Cytotoxicity test

We selected MDA-MB-231 as a model cell line for triple-negative breast cancer. This mammalian cell line is enriched with cancer stem cells, also known as "tumor-initiating cells," which play a pivotal role in cancer initiation, progression, and metastasis (Wang et al. 2020). These CSCs exhibit high expression of WNT beta-catenin signaling pathways, making them particularly suitable for evaluating β -catenin activity. In Fig. 7: A, the MTT assay demonstrates viability and inhibitory activity at 24 and 48 h. Our dose-response curve data indicates that increasing nanoparticle concentration in T2 resulted in a proportional decrease in cell viability, following a linear equation ($f(x) = x$) (Chandrasekaran et al. 2021). Based on the dose-response curve analysis: for L3, approximately half of the concentrations show no significant effect on cell viability, indicating a plateau effect described by a constant function ($f(x) = 2$). As the concentration increases beyond this point, viability decreases following a typical linear equation. In Figure S5, T2 exhibits an IC₅₀ of 1.88 ± 0.24 $\mu\text{g/ml}$ for 24 h, and 0.93 ± 0.11 $\mu\text{g/ml}$ for 48 h. L3 demonstrates an IC₅₀ of 30.6 ± 2.1 $\mu\text{g/ml}$ for 24 h, and 17.2 ± 0.98 $\mu\text{g/ml}$ for 48 h. These findings suggest varying sensitivity to the sample concentrations between T2 and L3 over different periods.

HRTEM of cells

The TEM micrographs in Fig. 8 illustrate that T2 nanoparticles (19 nm, individual particles) enter cells similarly to other small nanomaterials, likely through cellular membrane pores. They are distributed evenly throughout the cell, consistent with previous studies on uranium uptake (Muller et al. 2008). In contrast, L3 nanoparticles (50 nm, plasmon-coupled particles) enter cells via endocytosis, a process where the cellular membrane engulfs exogenous material to form vesicles within the cytoplasm. Endocytosis includes three types: phagocytosis, pinocytosis (fluid endocytosis or cell drinking), and receptor-mediated endocytosis. For nanoparticles like L3 (plasmon-coupled particles), their proximity and binding through electrical and magnetic forces (plasmon coupling) facilitate entry into cells in a manner analogous to how liquids are taken up during pinocytosis. This mechanism involves the formation of vesicles that merge with lysosomes within the cell, where the encapsulated material undergoes hydrolysis and processing (Albanese et al. 2012).

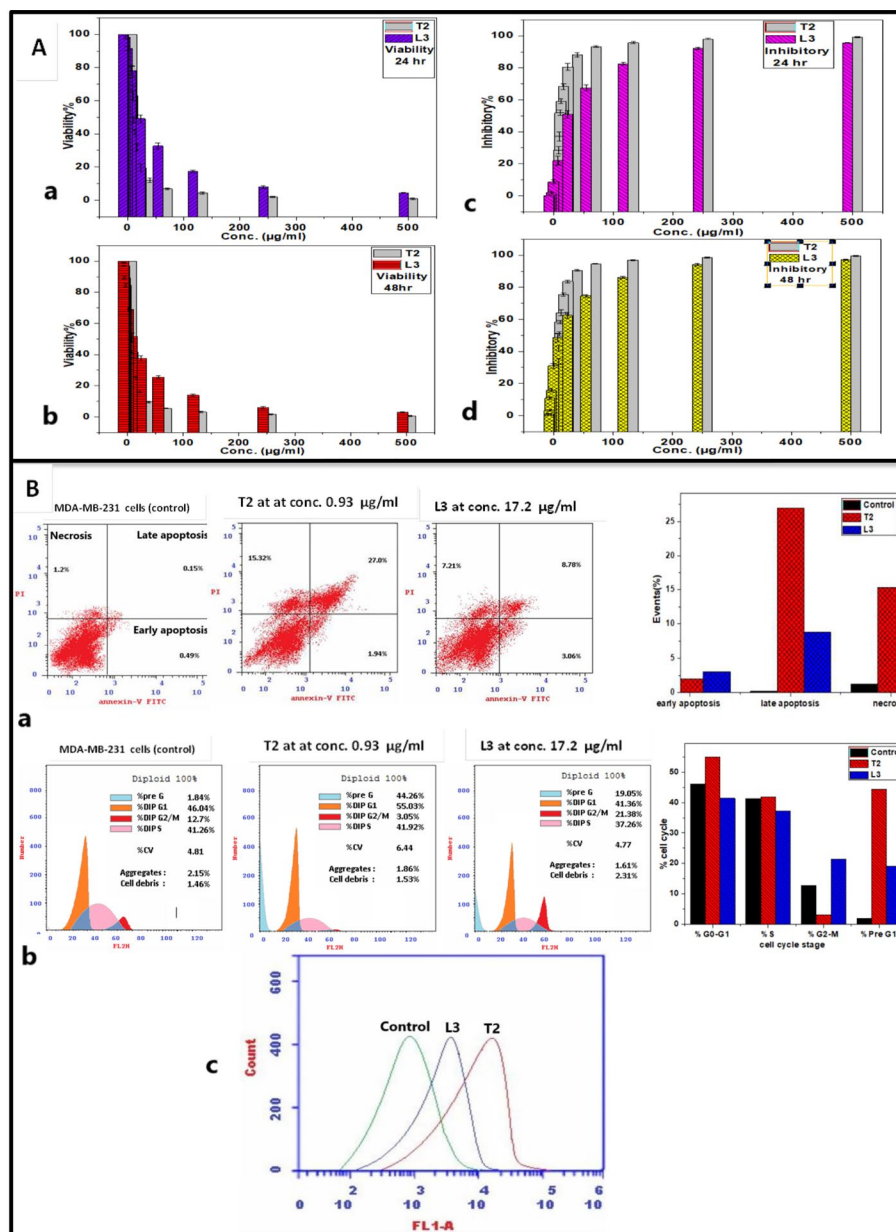


Fig. 7 A MTT assay “cytotoxicity test” on MDA-MB-231 cell line for T2, L3 samples. First **a, c** viability and inhibitory for 24 h. Second **b, d** viability and inhibitory for 48 h. B Flow cytometric data, **a** apoptosis, **b** cell cycle, **c** ROS

Flow cytometry data a: for apoptosis

From the analysis in Fig. 7B, it was observed that T2 induces apoptosis predominantly in the late apoptosis and necrotic regions (27% and 15.32%, respectively), indicating its higher toxicity. Conversely, L3 predominantly induces early apoptosis (3.06%), with a lower percentage of late apoptosis (8.78%) and almost no observed necrotic cells (Rahim et al. 2021). This suggests that L3 exhibits lower toxicity compared to T2 and is more effective in inducing apoptosis in a controlled manner.

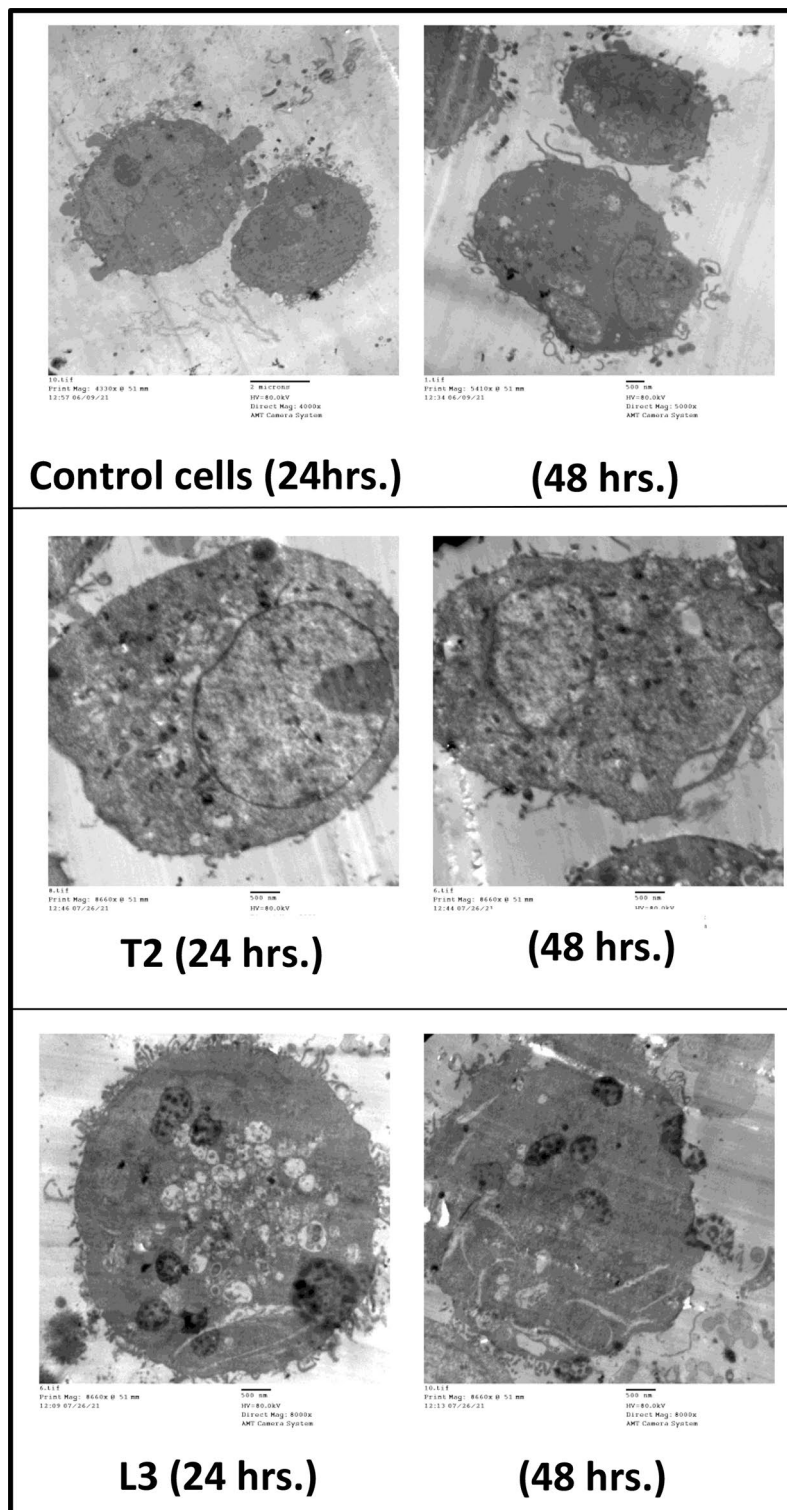


Fig. 8 TEM micrographs of MDA-MB-231 control cells, T2 and L3 incubated for 24, 48 h

Flow cytometry data b: for cell cycle

The cell cycle is a crucial process where cells replicate and divide, consisting of stages: G0, G1, S, G2, and M phases. Before entering the S phase, there's a checkpoint (checkpoint 1) that halts the cycle for repair upon detecting damage. If damage is irreparable, programmed cell death may occur. Mitosis occurs in the M phase, preceded by another important checkpoint (the M checkpoint). Anticancer drugs are categorized into two types: cell cycle-specific and non-specific. Cell cycle-specific drugs target particular phases of the cell cycle, affecting actively dividing cells like cancer cells while sparing cells in the G0 phase (non-dividing). This specificity makes them suitable for treating highly proliferative cancers. In contrast, cell cycle-non-specific drugs impact cells in any phase, including normal cells, potentially causing harm alongside cancer cell destruction (Verma et al. 2021; Mesmar et al. 2022). Based on Fig. 7B, it's hypothesized that T2 induces cell cycle arrest primarily at the G1/S phase transition, suggesting its mechanism involves interference at this checkpoint. Conversely, L3 appears to induce cell growth arrest predominantly at the G2/M phase transition. This suggests that L3 may be more effective against highly proliferative cancers such as leukemia and TNBC, while potentially being less harmful to normal cells compared to T2, which affects both cancer and normal cells significantly.

Flow cytometric data C: for reactive oxygen species

Reactive oxygen species (ROS) are free radicals, including peroxides, superoxides, and hydroxyl radicals, which when generated within cells, can cause damage to DNA, RNA, and proteins, ultimately leading to apoptotic cell death (Roy et al. 2017). In the context of cancer cell treatment with either T2 or L3, ROS formation was measured using flow cytometry (FL = 176762.407 for T2, 164754.366 for L3, and 127691.958 for MDA-MB-231 control cells). T2 treatment induced a significant increase in ROS levels, indicating a highly toxic effect. This treatment also resulted in cell cycle arrest predominantly at the G1/S phase, which suggests greater toxicity to normal cells alongside cancer cells compared to L3.

Apoptotic markers

Apoptosis is a normal physiologic programmed cell death needed for growth and development; it is a single cell death programmer other than the inflammatory way, which ends in necrosis and is regulated by the tumor suppressor gene P53. There are two apoptotic pathways: intrinsic and extrinsic. The intrinsic happens when DNA damage occurs. The extrinsic arises from an external signal. According to our western blot analysis data, we observed that T2-treated cells exhibited higher expression levels of BAX, Bcl-2 (Ko et al. 2022), Cytochrome c (Cyt c), caspase-3, caspase-9, and p53 compared to L3-treated cells. However, Bcl-2 showed lower expression in T2-treated cells compared to L3-treated cells. These findings indicate that both T2 and L3 are effective in inducing apoptosis in MDA-MB-231 cancer cells through the intrinsic apoptotic pathway (Table S6).

Inside the nucleus, β -catenin interacts with the TCF-LEF family of transcription factors, acting either as an enhancer or suppressor depending on the associated proteins. This interaction leads to the activation of specific genes crucial for cancer cell

growth, maintenance, proliferation, and metastasis. Examples of genes activated by β -catenin include c-Myc (Kamran et al. 2023), Cyclin D1 (Jun et al. 2023), Fibronectin, and Vimentin. c-Myc: functions as a regulatory protein involved in the transcription of genes essential for cancer cell proliferation. Cyclin D1: acts as a regulator of cyclin-dependent kinases, facilitating cell cycle progression through the G1/S checkpoint. When β -catenin translocates to the nucleus and activates these oncogenic pathways, it is considered an oncogene protein due to its role in promoting cancer progression and metastasis. The treatment of MDA-MB-231 cancer cells with either T2 or L3 resulted in decreased expression levels of β -catenin, c-Myc, and Cyclin D1 compared to the control, as shown in Fig. 9A. Interestingly, T2 exhibited stronger inhibition of β -catenin and c-Myc compared to L3. However, L3 showed a slightly higher inhibition of Cyclin D1 compared to T2. This suggests that while both treatments effectively reduce the expression of these proteins involved in cancer cell proliferation, T2 may be more effective against β -catenin and c-Myc, whereas L3 may have a stronger impact on Cyclin D1 inhibition. This combination could potentially lead to a synergistic effect in inhibiting cancer growth, particularly affecting cell cycle progression at the G1 phase.

In essence, the inhibition of Cyclin D1 and c-Myc by L3 in cancer cells prevents them from progressing beyond the G1 phase of the cell cycle. Cyclin D1 is crucial for regulating the transition from the G1 to the S phase (Lecarpentier et al. 2019), while c-Myc enhances Cyclin D1's activity during the G1 phase, as previously discussed. Based on the normalized ratios to β -actin provided in Table S7 (0.44 for T2 and 0.42 for L3), both T2 and L3 effectively reduce the expression of these key proteins involved in cell cycle regulation. This indicates their potential to inhibit cancer cell proliferation by preventing progression beyond the G1 phase, crucial for cell division and growth.

Vascular endothelial growth factor “VEGF” and DNA fragmentation data

The treatment of cancer cells with T2, which has an IC₅₀ of 68.73 ± 5.19 $\mu\text{g/ml}$, resulted in greater inhibition of VEGF expression compared to L3, which has an IC₅₀ of 475.86 ± 23.74 $\mu\text{g/ml}$ (Fig. 9B). This suggests that T2 is more effective in reducing VEGF expression in MDA-MB-231 cancer cells compared to L3. Furthermore, the treatment of MDA-MB-231 cancer cells with either T2 or L3 did not demonstrate any degradative effects or DNA cleavage as observed by gel electrophoresis. This was consistent across experiments where fixed concentrations of DNA were treated with varying concentrations of samples or fixed concentrations of samples were treated with varying concentrations of DNA (Fig. 9C). The observation that T2 enters the nucleus more effectively than L3, likely due to its smaller size (19 nm) and the plasmon coupling of L3 which reduces its nuclear pore passage, is notable. Despite this, both T2 and L3 were found to be non-genotoxic in our study. This contrasts with findings by Kimberly S. Butler et al., who investigated the mutagenicity of silver nanoparticles (AgNPs) of various sizes compared to silver nitrate. They reported that smaller AgNPs tend to be more genotoxic, primarily attributed to the release of silver ions. In Butler et al.'s study, silver ions released from AgNPs were found to interact with thiol groups on proteins and chelate with enzymes, rendering them more mutagenic than the

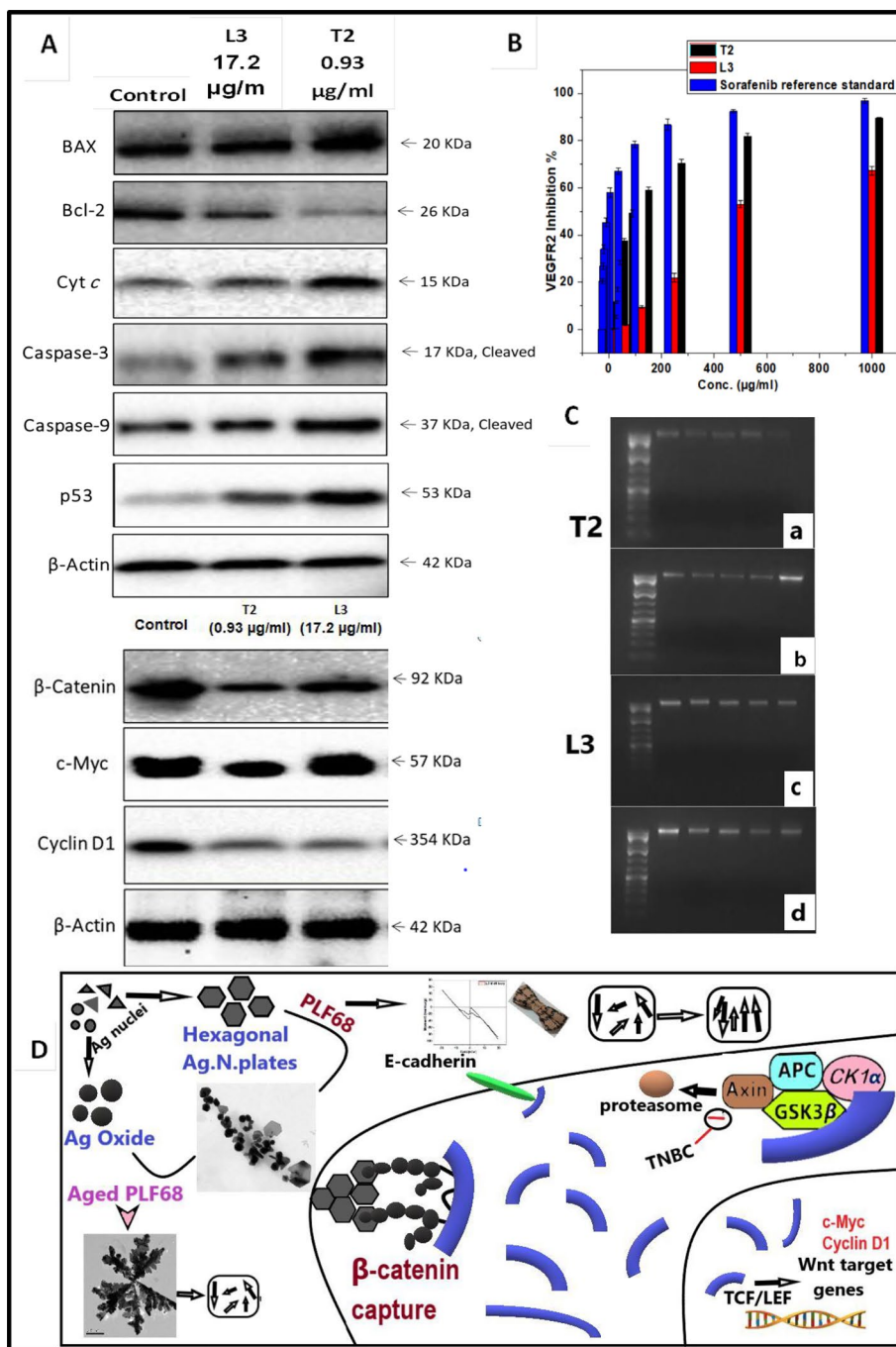


Fig. 9 **A** Western plot analysis of the apoptotic markers and β -catenin pathway proteins. **B** VEGF inhibition columns. **C** DNA fragmentation data by gel electrophoresis. **a, c** at fixed concentration Of DNA with different conc. Of samples. **b, d** at fixed conc. of samples with different conc. of DNA. **D** Graphical abstract of the whole paper

nanoparticles themselves. Therefore, any factors influencing the release of silver ions from nanoparticles can affect their mutagenicity. This underscores the importance of understanding nanoparticle characteristics, including size and surface properties, in evaluating their biological effects and potential genotoxicity (Butler et al. 2015).

Conclusion

L3 nanoparticles are plasmon-coupled Ag/Ag₂O nanoparticles designed to specifically target triple-negative breast cancer (TNBC) cells effectively. They feature a unique composite structure: a hexagonal mat of Ag₂O nanoparticles with spherical–cubic Ag nanoparticles coupled around it in circular and semi-circular formations. This design facilitates smooth entry into cancer cells through processes like "cell drinking" (pinocytosis). Key characteristics and effects of L3 nanoparticles include Cell Cycle Arrest: L3 nanoparticles induce cell cycle arrest at the G₂/M phase, preventing TNBC cells from progressing further in their division cycle. Reduced Cytotoxicity and ROS Levels: they effectively decrease cytotoxicity and reactive oxygen species (ROS) production compared to other treatments, minimizing damage to normal cells. Induction of Early Apoptosis: L3 nanoparticles promote early apoptosis in TNBC cells, facilitating programmed cell death before extensive damage occurs. Downregulation of β -catenin pathway: they reduce the expression of β -catenin and its pathway proteins, including Cyclin D1, which are critical for cancer cell proliferation and survival. Overall, L3 nanoparticles represent an innovative approach mimicking natural protein complexes involved in cellular degradation processes. They demonstrate targeted efficacy against TNBC while sparing normal cells, making them a promising candidate for the treatment of this aggressive cancer type.

Supplementary Information

The online version contains supplementary material available at <https://doi.org/10.1186/s12645-024-00292-0>.

Additional file 1.

Additional file 2.

Author contributions

S.I., Saad M and Ahmed G planned for the research work, A.Kamal carried out the experimental work, wrote the main manuscript text. All authors reviewed, revised and supervised the work.

Funding

Open access funding provided by The Science, Technology & Innovation Funding Authority (STDF) in cooperation with The Egyptian Knowledge Bank (EKB). No funds were received for this work.

Availability of data and materials

No datasets were generated or analysed during the current study.

Declarations

Competing interests

The authors declare no competing interests.

Received: 26 November 2023 Accepted: 18 September 2024

Published online: 23 October 2024

References

- Abdullah NISB, Ahmad MB, Shameli K (2015) Biosynthesis of silver nanoparticles using *Artocarpus elasticus* stem bark extract. *Chem Central J*. <https://doi.org/10.1186/s13065-015-0133-0>
- Ahmed Al-Thabaiti S et al (2013) Effects of surfactant and polymer on the morphology of advanced nanomaterials in aqueous solution. *Int J Electrochem Sci*. [https://doi.org/10.1016/S1452-3981\(23\)14014-4](https://doi.org/10.1016/S1452-3981(23)14014-4)
- Albanese A, Tang PS, Chan WCW (2012) The effect of nanoparticle size, shape, and surface chemistry on biological systems. *Ann Rev Biomed Eng*. <https://doi.org/10.1146/annurev-bioeng-071811-150124>
- Algahtani FD et al (2022) Development of ternary nanocomposites based on hydroxyapatite/silver oxide for biomedical applications: morphology, structure and antibacterial activity. *J Mater Res Technol* 20:60–72. <https://doi.org/10.1016/j.jmrt.2022.07.015>

- Arve K et al (2006) Structure—activity relationship in HC-SCR of NO_x by TEM, O₂-Chemisorption, and EDXS study of Ag/Al₂O₃. *J Phys Chem B* 110(1):420–427
- Burda C et al (2005) Chemistry and properties of nanocrystals of different shapes. *Chem Rev.* <https://doi.org/10.1021/cr030063a>
- Butler KS et al (2015) Silver nanoparticles: correlating nanoparticle size and cellular uptake with genotoxicity. *Mutagenesis* 30(4):577–591. <https://doi.org/10.1093/mutage/gev020>
- Cha H et al (2016) Plasmon coupling between silver nanoparticles: Transition from the classical to the quantum regime. *J Colloid Interface Sci* 464:18–24. <https://doi.org/10.1016/j.jcis.2015.11.009>
- Chandrasekaran J et al (2021) An in vitro study on the reversal of epithelial to mesenchymal transition by brusatol and its synergistic properties in triple-negative breast cancer cells. *J Pharm Pharmacol* 73(6):749–757. <https://doi.org/10.1093/jpp/rgab018>
- Cheng X et al (2019) Therapeutic potential of targeting the Wnt/β-catenin signaling pathway in colorectal cancer. *Biomed Pharmacother.* <https://doi.org/10.1016/j.biopha.2018.11.082>
- Dittmer J (2018) Breast cancer stem cells: features, key drivers and treatment options. *Seminars Cancer Biol.* <https://doi.org/10.1016/j.semcancer.2018.07.007>
- Geng B et al (2017) Ag₂O nanoparticles decorated hierarchical Bi₂MoO₆ microspheres for efficient visible light photocatalysts. *J Alloys Compounds* 699:783–787. <https://doi.org/10.1016/j.jallcom.2016.12.338>
- Han Y et al (2021) Large-area surface-enhanced Raman spectroscopy substrate by hybrid porous GaN with Au/Ag for breast cancer miRNA detection. *Appl Surface Sci.* <https://doi.org/10.1016/j.apsusc.2020.148456>
- Haq S et al (2018) Fabrication of pure and moxifloxacin functionalized silver oxide nanoparticles for photocatalytic and antimicrobial activity. *J Photochem Photobiol B Biol* 186:116–124. <https://doi.org/10.1016/j.jphotobiol.2018.07.011>
- Hassanpour S et al (2019) A novel paper based immunoassay of breast cancer specific carbohydrate (CA 15.3) using silver nanoparticles-reduced graphene oxide nano-ink technology: a new platform to construction of microfluidic paper-based analytical devices (μPADs) towards biomedical analysis. *Microchemical J* 146:345–358. <https://doi.org/10.1016/j.microc.2019.01.018>
- Hosseinpour-Mashkani SM, Ramezani M (2014) Silver and silver oxide nanoparticles: synthesis and characterization by thermal decomposition. *Mater Lett* 130:259–262. <https://doi.org/10.1016/j.matlet.2014.05.133>
- Huang X, Neretina S, El-Sayed MA (2009) Gold nanorods: from synthesis and properties to biological and biomedical applications. *Adv Mater.* <https://doi.org/10.1002/adma.200802789>
- Huang WC et al (2019) Sophoraflavanone G from *Sophora flavescens* induces apoptosis in triple-negative breast cancer cells. *Phytomedicine.* <https://doi.org/10.1016/j.phymed.2019.152852>
- Ito A, Honda H, Kobayashi T (2006) Cancer immunotherapy based on intracellular hyperthermia using magnetite nanoparticles: A novel concept of “heat-controlled necrosis” with heat shock protein expression. *Cancer Immunol Immunother.* <https://doi.org/10.1007/s00262-005-0049-y>
- Jain PK, El-Sayed MA (2010) Plasmonic coupling in noble metal nanostructures. *Chem Phys Lett* 487(4–6):153–164. <https://doi.org/10.1016/j.cplett.2010.01.062>
- Jinu U et al (2017) Biofabrication of cubic phase silver nanoparticles loaded with phytochemicals from solanum nigrum leaf extracts for potential antibacterial, antibiofilm and antioxidant activities against MDR human pathogens. *J Cluster Sci* 28(1):489–505. <https://doi.org/10.1007/s10876-016-1125-5>
- Joseph V et al (2011) A simple approach to the synthesis of hexagonal-shaped silver nanoplates. *J Nanomater.* <https://doi.org/10.1155/2011/825637>
- Juganson K et al (2015) NanoE-Tox: new and in-depth database concerning ecotoxicity of nanomaterials. *Beilstein J Nanotechnol* 6(1):1788–1804. <https://doi.org/10.3762/bjnano.6.183>
- Jun SY et al (2023) Prognostic potential of cyclin D1 expression in colorectal cancer. *J Clin Med.* <https://doi.org/10.3390/jcm12020572>
- Kamran DE, Hussain M, Mirza T (2023) Investigating in situ expression of c-MYC and candidate ubiquitin-specific proteases in DLBCL and assessment for peptidyl disruptor molecule against c-MYC-USP37 complex. *Molecules.* <https://doi.org/10.3390/molecules28062441>
- Kaplan Ö et al (2022) Biosynthesis and characterization of silver nanoparticles from *Tricholoma ustale* and *Agaricus arvensis* extracts and investigation of their antimicrobial, cytotoxic, and apoptotic potentials. *J Drug Delivery Sci Technol.* <https://doi.org/10.1016/j.jddst.2022.103178>
- Ko EB et al (2022) Gallic Acid hindered lung cancer progression by inducing cell cycle arrest and apoptosis in A549 lung cancer cells via PI3K/Akt pathway. *Biomol Ther* 30(2):151–161. <https://doi.org/10.4062/biomolther.2021.074>
- Korkmaz N, Karadağ A (2021) Microwave assisted green synthesis of ag, ag₂o, and ag₂o₃ nanoparticles. *J Turkish Chem Soc Sec A Chem* 8(2):585–592. <https://doi.org/10.18596/jotcsa.784065>
- Le Trong H et al (2017) Paramagnetic behaviour of silver nanoparticles generated by decomposition of silver oxalate. *Solid State Sci* 69:44–49. <https://doi.org/10.1016/j.solidstatesciences.2017.05.009>
- Lecarpentier Y et al (2019) Multiple targets of the canonical WNT/β-catenin signaling in cancers. *Front Oncol* 9(November):1–17. <https://doi.org/10.3389/fonc.2019.01248>
- Lotfy WA et al (2021) Biosynthesis of silver nanoparticles by *aspergillus terreus*: characterization, optimization, and biological activities. *Front Bioeng Biotechnol.* <https://doi.org/10.3389/fbioe.2021.633468>
- Mesmar J et al (2022) Ethanolic extract of *Origanum syriacum* L. leaves exhibits potent anti-breast cancer potential and robust antioxidant properties. *Front Pharmacol.* <https://doi.org/10.3389/fphar.2022.994025>
- Muller DS et al (2008) Role of the sodium-dependent phosphate cotransporters and absorptive endocytosis in the uptake of low concentrations of uranium and its toxicity at higher concentrations in LLC-PK1 cells. *Toxicol Sci* 101(2):254–262. <https://doi.org/10.1093/toxsci/kfm266>
- Rahim NFC et al (2021) Cytotoxicity and apoptosis effects of curcumin analogue (2E,6E)-2,6-Bis(2,3-Dimethoxybenzylidene) cyclohexanone (DMCH) on human colon cancer cells HT29 and SW620 in vitro. *Molecules.* <https://doi.org/10.3390/molecules26051261>

- Raju NR, Kumar KJ, Subrahmanyam A (2009) Physical properties of silver oxide thin films by pulsed laser deposition: effect of oxygen pressure during growth. *J Phys D Appl Phys*. <https://doi.org/10.1088/0022-3727/42/13/135411>
- Ramesh MNV et al (2007) Reactively radio frequency sputtered silver oxide thin films: phase evolution and phase stability. *Mod Phys Lett B* 21(28):1933–1944
- Rana MA et al (2019) Interplay of Wnt β -catenin pathway and miRNAs in HBV pathogenesis leading to HCC. *Clin Res Hepatol Gastroenterol*. <https://doi.org/10.1016/j.clinre.2018.09.012>
- Roy A et al (2017) Induction of mitochondrial apoptotic pathway in triple negative breast carcinoma cells by methylglyoxal via generation of reactive oxygen species. *Mol Carcinogenesis* 56(9):2086–2103. <https://doi.org/10.1002/mc.22665>
- Salahandish R et al (2018) Nano-biosensor for highly sensitive detection of HER2 positive breast cancer. *Biosens Bioelectr* 117:104–111. <https://doi.org/10.1016/j.bios.2018.05.043>
- Sophia PJ et al (2020) Solar induced photocatalytic degradation of methylene blue by CdS/Ag₂O nanocomposites. *ChemistrySelect* 5(14):4125–4135. <https://doi.org/10.1002/slct.202000475>
- Suber L (2018) Formation and oriented aggregation of tabular hexagonal silver particles. *Condensed Matter* 3(2):1–10. <https://doi.org/10.3390/condmat3020013>
- Syed B, Nagendra Prasad MN, Satish S (2019) Synthesis and characterization of silver nanobactericides produced by *Aneurinibacillus migulanus* 141, a novel endophyte inhabiting *Mimosa pudica* L. *Arabian J Chem* 12(8):3743–3752. <https://doi.org/10.1016/j.arabjc.2016.01.005>
- Tang S et al (2009) PVP-assisted sonoelectrochemical growth of silver nanostructures with various shapes. *Mater Chem Phys* 116(2–3):464–468. <https://doi.org/10.1016/j.matchemphys.2009.04.004>
- Tanimoto H, Hashiguchi K, Ohmura S (2015) Growth Inhibition of hexagonal silver nanoplates by localized surface plasmon resonance. *J Phys Chem C* 119(33):19318–19325. <https://doi.org/10.1021/acs.jpcc.5b04664>
- Tawfik WZ et al (2018) Outstanding features of Cu-doped ZnS nanoclusters. *Nanotechnology*. <https://doi.org/10.1088/1361-6528/aab4d1>
- Toropov NA, Leonov NB, Vartanyan TA (2018) Influence of silver nanoparticles crystallinity on localized surface plasmons dephasing times. *Phys Status Solidi B Basic Res*. <https://doi.org/10.1002/pssb.201700174>
- Tseng CC et al (2010) Effects of deposition and annealing temperatures on the electrical and optical properties of Ag₂O and Cu₂O–Ag₂O thin films. *J Vacuum Sci Technol A Vacuum Surfaces Films* 28(4):791–794. <https://doi.org/10.1116/1.3425638>
- Tu CY, Wu JM (2021) Localized surface plasmon resonance coupling with piezophototronic effect for enhancing hydrogen evolution reaction with Au@MoS₂ nanoflowers. *Nano Energy*. <https://doi.org/10.1016/j.nanoen.2021.106131>
- Verma P et al (2021) Induction of microtubule hyper stabilization and robust G₂/M arrest by N-4-CN in human breast carcinoma MDA-MB-231 cells. *Fundamental Clin Pharmacol* 35(6):955–967. <https://doi.org/10.1111/fcp.12660>
- Vittorio O et al (2011) Magnetic carbon nanotubes: a new tool for shepherding mesenchymal stem cells by magnetic fields. *Nanomedicine* 6(1):43–54. <https://doi.org/10.2217/nnm.10.125>
- Wahab R et al (2019) Gold quantum dots impair the tumorigenic potential of glioma stem-like cells via β -catenin down-regulation in vitro. *Int J Nanomed* 14:1131–1148. <https://doi.org/10.2147/IJN.S195333>
- Wang XH et al (2020) HMGB1 promotes the proliferation and metastasis of lung cancer by activating the Wnt/ β -catenin pathway. *Technol Cancer Res Treat*. <https://doi.org/10.1177/1533033820948054>
- Wong SHM et al (2018) E-cadherin: its dysregulation in carcinogenesis and clinical implications. *Crit Rev Oncol Hematol*. <https://doi.org/10.1016/j.critrevonc.2017.11.010>
- Xiong Y, Xia Y (2007) Shape-controlled synthesis of metal nanostructures: the case of palladium. *Adv Mater* 19(20):3385–3391. <https://doi.org/10.1002/adma.200701301>
- Xu J et al (2015) β -catenin is required for the tumorigenic behavior of triple-negative breast cancer cells. *PLoS ONE*. <https://doi.org/10.1371/journal.pone.0117097>
- Xu W et al (2017) Abnormal oxidation of Ag films and its application to fabrication of photocatalytic films with a-TiO₂/h-Ag₂O heterostructure. *J Phys Chem C* 121(18):9901–9909. <https://doi.org/10.1021/acs.jpcc.7b01229>
- Yoo Y, Kim M, Kim B (2021) Epitaxially integrated hierarchical ZnO/Au/SrTiO₃ and ZnO/Ag/Al₂O₃ heterostructures: three-dimensional plasmo-photonic nanoarchitecturing. *Nanomaterials*. <https://doi.org/10.3390/nano11123262g>
- Yu W et al (2020) Targeting β -catenin signaling by natural products for cancer prevention and therapy. *Front Pharmacol* 11(June):1–12. <https://doi.org/10.3389/fphar.2020.00984>

Publisher's Note

Springer Nature remains neutral with regard to jurisdictional claims in published maps and institutional affiliations.